

Impact of Aerosol Intrusions on Arctic Boundary Layer Clouds. Part I: 4 May 1998 Case

G. G. CARRIÓ, H. JIANG, AND W. R. COTTON

Department of Atmospheric Science, Colorado State University, Fort Collins, Colorado

(Manuscript received 24 June 2003, in final form 2 August 2004)

ABSTRACT

The objective of this paper is to assess the impact of the entrainment of aerosol from above the inversion on the microphysical structure and radiative properties of boundary layer clouds. For that purpose, the Los Alamos National Laboratory sea ice model was implemented into the research and real-time versions of the Regional Atmospheric Modeling System at Colorado State University.

A series of cloud-resolving simulations have been performed for a mixed-phase Arctic boundary layer cloud using a new microphysical module that considers the explicit nucleation of cloud droplets. Different aerosol profiles based on observations were used for initialization. When more polluted initial ice-forming nuclei (IFN) profiles are assumed, the liquid water fraction of the cloud decreases while the total condensate path, the residence time of the ice particles, and the downwelling infrared radiation monotonically increase. Results suggest that increasing the aerosol concentrations above the boundary layer may increase sea ice melting rates when mixed-phase clouds are present.

1. Introduction

It has long been known that there are major intrusions of polluted air into the Arctic basin and that they often contain high concentrations of cloud condensation nuclei (CCN; Borys and Rahn 1981; Patterson et al. 1982). The surface energy budget over the Arctic basin is strongly controlled by low-level cloudiness, its behavior, and its interactions with the sea ice/ocean system (Curry et al. 2000; Perovich et al. 1999). Moreover, during the recent Surface Heat Budget of the Arctic (SHEBA) spring field campaign, the air mass was found to be moderately polluted in terms of CCN and ice-forming nuclei (IFN) concentrations above the boundary layer and extremely clean below on several occasions. Several cloud-resolving and large-eddy simulation (LES) modeling studies of Arctic stratus clouds have revealed that these cloud systems are quite vulnerable to even modest changes in CCN and IFN concentrations (Olsson et al. 1998; Harrington et al. 1999; Olsson and Harrington 2000; Jiang et al. 2000).

Jiang et al. (2001) conducted two sets of three-dimensional simulations of a springtime Arctic boundary layer cloud observed during the SHEBA 1998 spring Intensive Operation Period (IOP) on 18 May 1998 to study the influence of entrainment of CCN at cloud top on the cloud microphysical and dynamical structure, radiative properties, and cloud evolution. The above-mentioned study was run with explicit representation of the CCN spectrum and cloud droplet spectrum. The initial CCN concentration was a constant value of 30 cm^{-3} in the control run, while it varied from 30 cm^{-3} below cloud base to a peak of 250 cm^{-3} at the inversion in the sensitivity run, similar to the airborne observed values. Results from the sensitivity run show that droplet concentrations increase about twofold, effective radii decrease by 9% to 15% from cloud top to cloud base, liquid water content increases about 21%, and no drizzle reached the ground in comparison with the control run. The dynamic response becomes significant by the end of the 5-h simulation, as reflected in more vigorous eddies in the sensitivity run. The response of the cloud optical properties to entrainment occurs from the beginning of the simulations. Cloud albedo increases 12%, while cloud optical depth increases 33%. These results are consistent with both observations and modeling studies. Unfortunately the case studied by Jiang et al. (2001) was too warm to

Corresponding author address: Gustavo Gabriel Carrió, Atmospheric Science Building, Office 225, Colorado State University, Fort Collins, CO 80523.
E-mail: carriog@atmos.colostate.edu

examine the impact of entrained IFN on the cloudy boundary layer.

In this paper, we present a series of sensitivity numerical experiments based on a colder case that was extensively observed during SHEBA. This mixed-phase boundary layer cloud occurred on 4 May 1998 at the SHEBA site (approximately 76°N, 165°W). A two-dimensional fine resolution version of the Regional Atmospheric Modeling System at Colorado State University (RAMS@CSU) was used for this modeling study. The Los Alamos National Laboratory sea ice model (Hunke and Lipscomb 1999) was implemented into RAMS@CSU and modified in its structure to allow module communication in an interactive multigrid framework. To isolate the effect of aerosol entrainment from above the inversion, several cloud-resolving model (CRM) simulations were performed assuming different initial profiles within the upper layer. Observed IFN and CCN profiles for the above-mentioned case (Rogers et al. 2001; Yum and Hudson 2001) were used as benchmarks to design the sensitivity experiments. All simulations were performed using the two-moment microphysical treatment that predicts mixing ratios and number concentrations for all species. A brief description of the new model is given section 2. Section 3 considers the design of the numerical sensitivity experiments and general simulation conditions. Results, and summary and conclusions are presented in sections 4 and 5, respectively.

This study is meant to be a theoretical investigation rather than a realistic simulation of a particular case. Multiple remote sensing measurements (35-GHz cloud radar, depolarization lidar, microwave radiometer) clearly indicated the presence of an upper-layer cloud that extended up to 5000 m. Significant sedimentation from the upper cloud into the lower cloud was documented. Radar data could not clearly distinguish separate low and upper clouds due to the sedimentation of ice particles (see Zuidema et al. 2005). Therefore, the presence of this upper cloud imposes a limitation to simulate its radiative and microphysical effects, as the model domain used for these numerical experiments is approximately 3300-m deep. The objective of the present paper is to access the impact of the entrainment of aerosols (CCN and IFN) at cloud top on the microstructure of Arctic boundary layer clouds. A follow-up paper (Carrió et al. 2005, hereafter Part II) evaluates the potential effects of enhanced aerosol concentrations above the inversion on sea ice melting rates during a spring–summer period. We performed a series of multimonth CRM simulations using 2 to 3 daily SHEBA soundings to provide time-evolving boundary conditions.

2. Model description

The dynamical modeling framework used for this study is RAMS@CSU (Pielke et al. 1992; Cotton et al. 2003) in its two-dimensional eddy-resolving version. This nonhydrostatic model integrates predictive equations for the wind components, the Exner function, the ice liquid water potential, and the total mixing ratio on a vertically stretched Arakawa C grid. The model used in this study is the same dynamic model used in Jiang et al. (2001) except that this version includes a complex bulk microphysical module and the sea ice module.

a. Treatment of the microphysics

In the two-moment microphysical framework (Meyers et al. 1997), both mass mixing ratio and number concentrations of the hydrometeor species are predicted. The hydrometeor size spectrum is assumed a gamma distribution function. The new microphysical module (Saleeby and Cotton 2004), among other new features, considers the nucleation of cloud droplets based on the activation of CCN and a bimodal description for the cloud droplet size distribution. The introduction of prognostic cloud droplet concentration via nucleation of CCN limits the amount of cloud water depending on the available CCN. This eliminates the highly limiting constraints of selecting a mean diameter for cloud droplets or a constant number concentration. CCN (and giant CCN) are activated for nucleation of cloud droplets based on look-up tables derived from a Lagrangian model developed by Feingold and Heymsfield (1992). The consideration of a large cloud droplet mode, in combination with the traditional single mode of cloud droplets, allows a more accurate representation of the bimodal distribution of cloud droplets that occurs in the atmosphere. The predicted microphysical categories also include the number concentration and mixing ratio of rain, pristine ice, snow, aggregates graupel and hail, as well as the IFN and CCN concentration. IFN can be defined as a vertically and/or horizontally heterogeneous variable that can be advected and diffused (Cotton et al. 2003). Snow is defined as larger pristine ice crystals ($>100 \mu\text{m}$), which have grown by vapor deposition and riming, while aggregates are defined as ice particles formed by collision and coalescence of pristine ice, snow, or other aggregates.

b. Two-stream radiation model

A two-stream radiative transfer model is used for this study (Harrington et al. 1999). The two-stream model solves the radiative transfer equations for three gaseous constituents, H_2O , O_3 , and CO_2 and the optical effects

of the hydrometeor size spectra. Gaseous absorption is calculated by following the fast exponential sum fitting of transmissions method proposed by Ritter and Geleyn (1992). The Lorenz–Mie theory is used to compute the optical properties for water drops, while the theory of Mitchell et al. (1996) is used for nonspherical ice crystals. For each hydrometeor species, the band-averaged values of optical properties are computed for the assumed gamma distribution used in RAMS following the method of Slingo and Schreckner (1982).

c. RAMS–CICE coupling

The Los Alamos sea ice model, CICE (Hunke and Lipscomb 1999), has been interfaced with the research and real-time versions of RAMS@CSU. The original version of CICE was modified in its structure to allow module communication in an interactive multigrid framework. Routines have been included to evaluate the surface momentum fluxes corresponding to each thickness category (and open sea), and various improvements have been made to provide more realistic turbulent surface fluxes and albedo over Arctic interior ice regions. Iterative methods that consider variable roughness lengths have been applied to evaluate momentum and heat fluxes. The saltation of snow is considered to evaluate the roughness lengths independently for each thickness category with non-negligible snow cover. Six ice thickness categories (with four internal layers) are considered to describe the subgrid-scale ice thickness distribution of each horizontal grid cell. The linear remapping scheme of Lipscomb (2001) is used to transfer ice among categories.

3. Experiment design and model grid structure

A mixed-phase cloud observed on 4 May 1998 during the First International Satellite Cloud Climatology Project (ISCCP) Regional Experiment (FIRE)/SHEBA field experiment was chosen for a sensitivity study. Airborne data for both IFN and CCN data for this Arctic boundary layer cloud were used to design the numerical experiments. The CCN data were collected during the FIRE–Arctic Cloud Project (ACE) project using the instantaneous CCN spectrometer of the Desert Research Institute (DRI). The concentrations of approximately 100 and 250 cm^{-3} (active at 1% supersaturation) are used for below and above the inversion, respectively (Yum and Hudson 2001). The IFN vertical profile derived from the CSU continuous flow diffusion chamber (CFDC) ice nucleus counter data, exhibits relatively large concentrations above the boundary layer with a maximum value of 85.6 L^{-1} (ac-

tive at 0.8% supersaturation), while below the inversion the vertical average is approximately 3 L^{-1} (Rogers et al. 2001).

This set of experiments places special emphasis on studying how the structure of the cloud is affected by the entrainment of aerosol from the polluted air layer overriding the inversion. The simulations were initialized with different initial IFN and CCN profiles based on those observations. In the control run we assumed constant clean profiles for IFN and CCN of 3 L^{-1} and 100 cm^{-3} , respectively. All other experiments were initialized with these clean aerosol concentrations within the boundary layer and the observed profiles multiplied by different factors. Figure 1 gives all IFN and CCN profiles that have been used to initialize the various runs. A summary of the numerical experiments that correspond to results presented in this paper is given in Table 1.

All the experiments have been performed in a two-dimensional (2D) framework. The simulation domain was 5000 m in the horizontal, 3325 m in the vertical, and approximately located at 76°N, 165°W. A constant horizontal grid spacing of 50 m and a time step of 2 s were used. The vertical grid was stretched using the relationship $\Delta z_{k+1} = 1.05 \Delta z_k$ with 30-m spacing at the finest to provide better resolution within the boundary layer. The lateral boundary conditions were cyclic and the domain top is a rigid lid. Rayleigh damping was used in the five highest levels of the domain to prevent the reflection of vertically traveling gravity waves off this rigid lid. Noninertial effects were neglected and CICE provided surface properties and fluxes. CICE was initialized with a mean thickness of 2.41 m that approximately corresponds to the average value of the seven gauges closest to the SHEBA site. The vertical profiles of temperature (T), relative humidity (RH), as well as the horizontal wind component (U) corresponding to the SHEBA of 2300 UTC 3 May 1998 were used to initialize all numerical experiments. The profiles of T , RH, and U used for initialization and those corresponding to the sounding of 0500 UTC 4 May 1998 are given in Fig. 2. At initialization time both T and RH exhibit a sharp increase between 900 and 1200 m, approximately. The boundary layer inversion altitude, as well as RH, significantly increase during the first hours of 4 May. To take into account the large-scale forcing during the simulation time, a Newtonian relaxation technique (nudging) is used to consider the large-scale tendencies. These nudging terms were based on the vertical profiles of T , RH, and horizontal wind component corresponding to four 4 May 1998 soundings (0515, 1115, 1715, and 2315 UTC). Nudging in this study takes the following form:

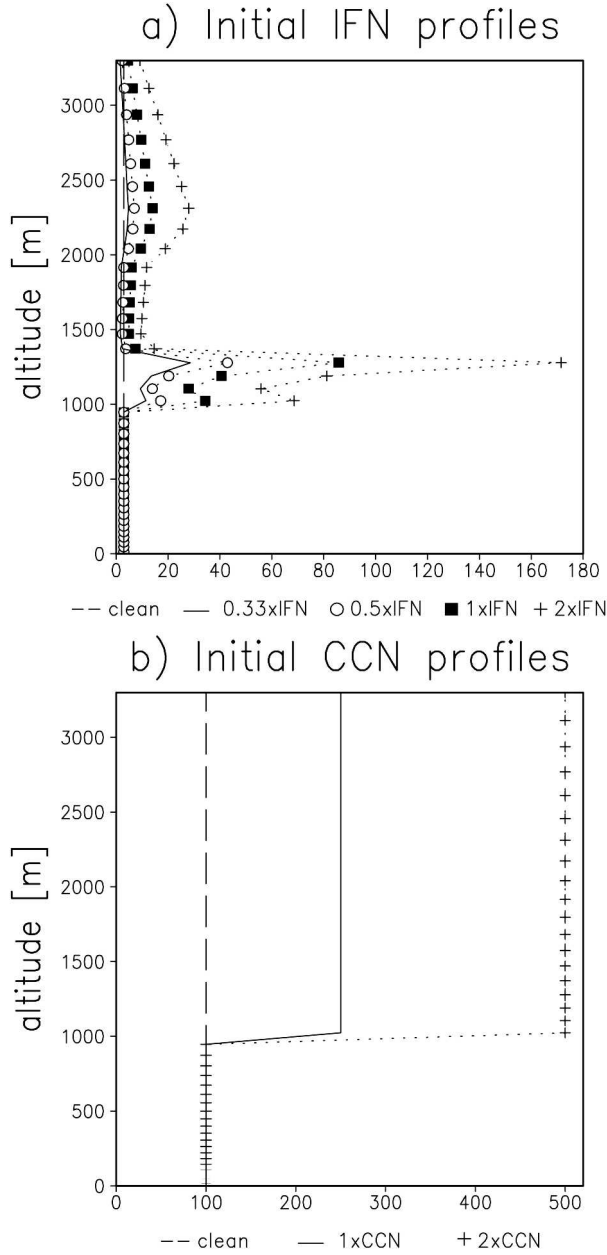


FIG. 1. IFN and CCN vertical profiles used for initialization in L^{-1} and cm^{-3} , respectively. Here, $1 \times$ IFN and $1 \times$ CCN denote the vertical IFN and CCN profiles associated to the observations.

$$\psi(k, i, t) = \psi(k, i, t - \Delta t) + \text{model} + [\psi_{\text{obs}}(k, t - \Delta t) - \psi H(k, t - \Delta t)/\tau], \quad (1)$$

where $\psi(k, i, t)$ is the predicted value of a nudged variable at the end of the current time step; $\psi(k, i, t - \Delta t)$ is the model value at the end of the previous time step; the model includes advection, diffusion, thermodynamic effects, etc.; $\psi_{\text{obs}}(k, t)$ is the vertical profile being nudged to and is a function of the vertical index k ;

TABLE 1. Initialization conditions.

Run	IFN	CCN
Control run	Clean	Clean
exp2	$0.33 \times$ IFN	Clean
exp3	$0.50 \times$ IFN	Clean
exp4	$1 \times$ IFN	Clean
exp5	$2 \times$ IFN	Clean
exp6	$1 \times$ IFN	$1 \times$ CCN
exp7	$1 \times$ IFN	$2 \times$ CCN

$\psi H(k, t - \Delta t)$ is the horizontal average of at the end of the previous time step, and τ denotes the time scale.

The values of ψ_{obs} used to nudge the horizontal wind component, total mixing ratio, potential temperature were evaluated from the above-mentioned SHEBA soundings by using a linear interpolation method and a value of 12 h for τ . This scheme takes into account the large-scale tendencies but avoids nudging out the fine-scale features developed in the CRM domain.

4. Results

The total simulation time of each numerical experiment was thirty hours. The first six hours were considered as spinup time and have not been utilized for comparisons. Some simulated microphysical profiles corresponding to the control run are compared with those initialized with observed IFN and CCN profiles above the inversion (exp6) in Figs. 3–5. Time–height cross sections of horizontally averaged values of the liquid water content (LWC) and ice water content (IWC) are given in Fig. 3. It can be seen that LWC plots (Figs. 3a and 3b) exhibit a common pattern of two maxima; one associated with the highest LWC values between 1800 and 2100 UTC, and a secondary one between 1200 and 1500 UTC. However, significantly lower values (less than 50%) were obtained for exp6. The plots of IWC that represents all solid species (i.e., pristine ice, snow, and aggregates) are given in Figs. 3c and 3d. Absolute IWC maxima occur at approximately the same time and altitude although, the magnitudes differ significantly ($\sim 50\%$). On the one hand, the area of large IWC values (with respect to the control run) has a higher vertical extension and exhibits a secondary maximum close to the inversion. On the other hand, this area is much wider as glaciation is less abrupt but starts earlier.

Time–height cross sections of simulated liquid effective radius (R_{eff}) for the control case and the exp6 are given in Figs. 4a and 4b, respectively. Simulated R_{eff} values were computed as the horizontally averaged ratio between the third- and second-order moments of the droplet size distributions. Figure 4c gives values of

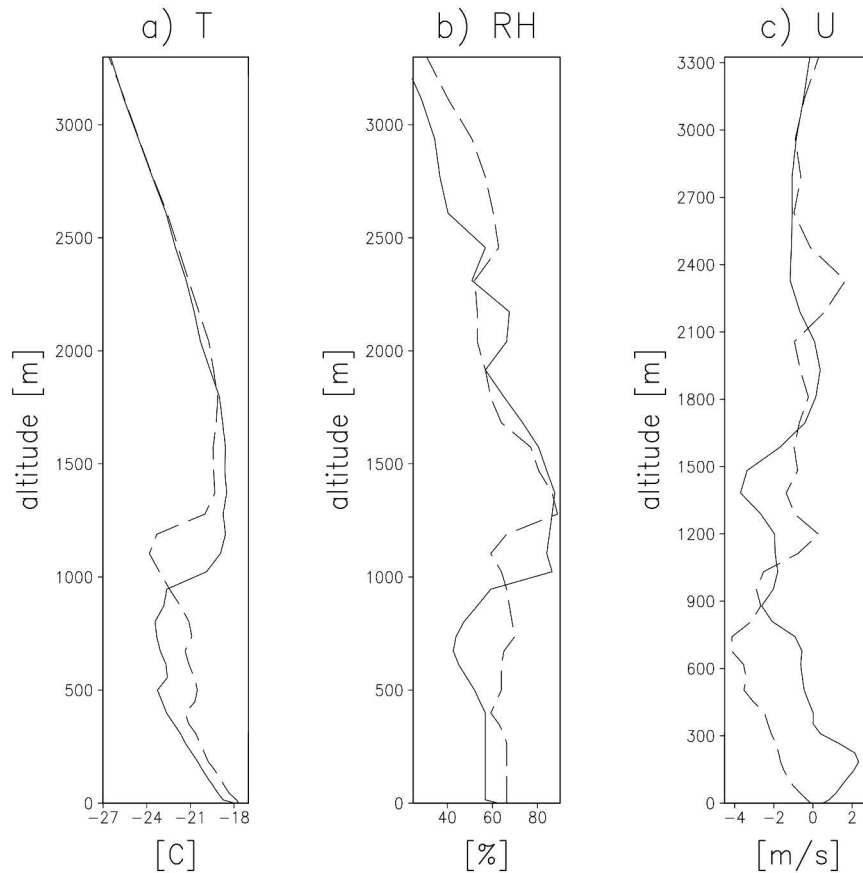


FIG. 2. Vertical profiles of temperature, relative humidity, and horizontal wind component. Solid lines and dashed lines denote soundings at initialization time and 6 h after, respectively.

Reff retrieved using surface-based remote sensors as well as aircraft observations at a 10-min resolution. Liquid cloud droplet sizes were estimated by combining liquid water contents, determined from an adiabatic ascent calculation and constrained by the liquid water paths retrieved from an upwardly pointing microwave radiometer, with the droplet concentrations and distribution widths determined from aircraft data [see Zuidema et al. (2005) for details]. The vertical profiles of Reff simulated for both runs exhibit a pattern similar to that of the observations.

Figure 5 is similar to Fig. 4 except for the total ice particle concentration (Ni). When comparing the simulated Ni values (Figs. 5a,b), differences are most important above 600 m after 1400 UTC while they are negligible before that time. Large differences associated with precipitating ice particles can be seen at lower levels of the cloud at approximately 2100 UTC. Radar-retrieved ice particle concentration is given in Fig. 5c. These values were retrieved by assuming that small ice particles are related to the larger ice particles according to an exponential size distribution. These retrieved con-

centrations are approximate, as assumptions on the impact of particle habit on radar reflectivity are also required. They have received little comparison to aircraft data, particularly in mixed-phase conditions, but some comparisons suggest the radar-estimated ice particle concentrations are likely to be underestimates (P. Zuidema 2004, personal communication). The main difference between the simulated and retrieved Ni values is that vertical depth of the layer with of nonzero values is much higher for the observations. This difference is linked to the sedimentation of ice particles from the upper cloud that was observed during 4 May until approximately 2200 UTC (see section 1). Simulated concentrations were also more variable with time and with altitude than the retrieved values. The run initialized with the observed IFN and CCN profiles above the inversion (exp6) exhibit maxima at times similar to those of the observations, however, simulated values were significantly higher.

To analyze the sensitivity to IFN entrainment from above the inversion, the control run was compared with those that assume a clean CCN profile but are initial-

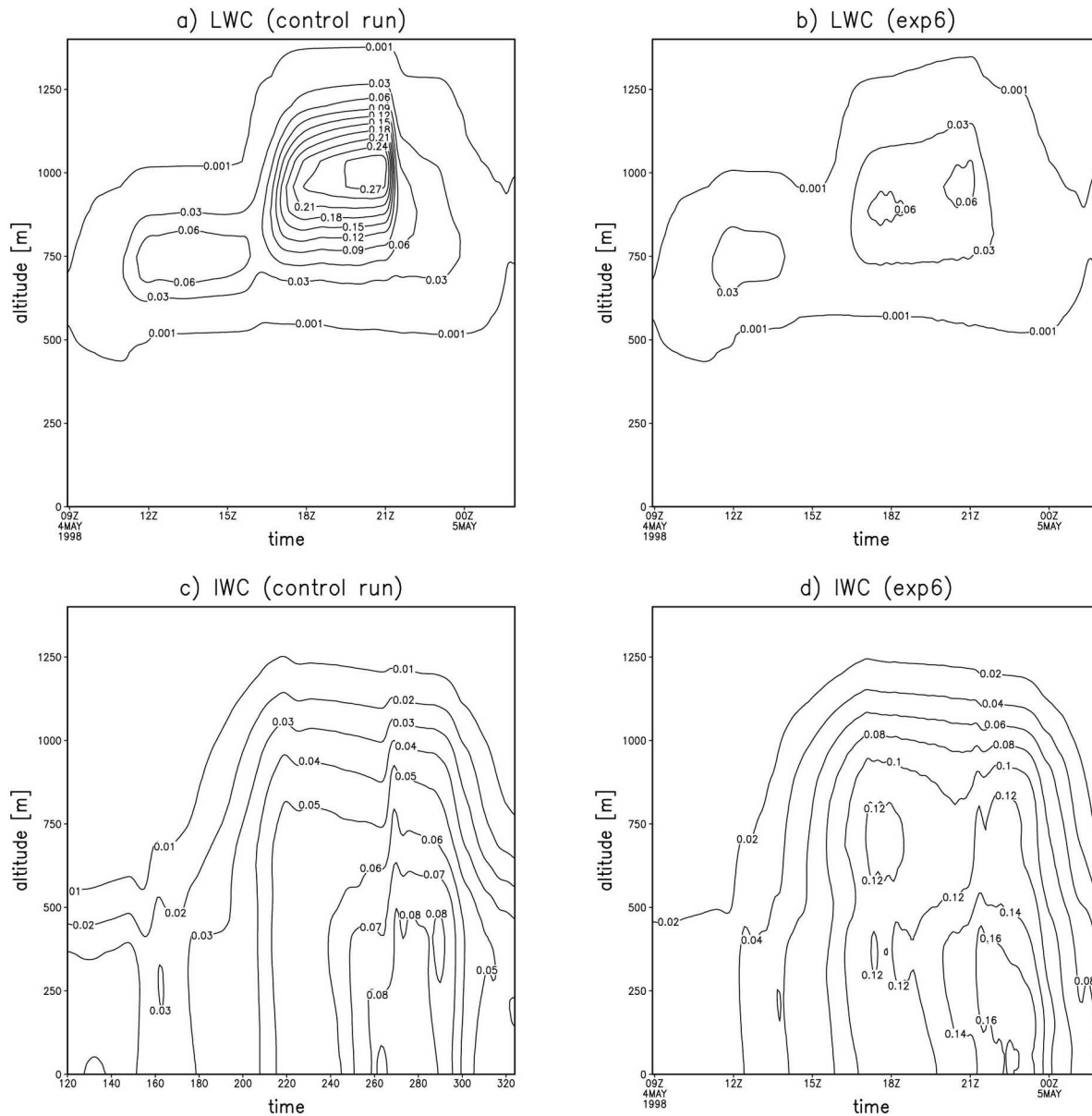


FIG. 3. Time series plots of horizontally averaged values of (a), (b) LWC and (c), (d) IWP for (a), (c) the control run and (b), (d) the run that corresponds to the observed aerosol concentrations (exp6).

ized with IFN profiles that correspond to the observed one multiplied by the factors 1/3, 1/2, 1, and 2 (exp2, exp3, exp4, and exp5, respectively). The time evolution of the horizontally averaged total condensate path (TCP) is shown in Fig. 6a. TCP is defined as the vertical integral of the total condensate. It can be seen that TCP monotonically increases when the initial IFN concentration above the inversion increases. The simulated liquid water paths also exhibit a monotonic behavior, decreasing for higher initial IFN concentrations within the upper layer (not shown). Figure 6b shows a time–

height cross section of horizontally averaged concentration of available IFN for the run initialized with the observed IFN profile. The 0.001 g m^{-3} LWC contour has been superimposed in this panel to indicate liquid cloud boundaries. Concentrations begin to significantly increase below the altitude of 1000 m after 1500 UTC, coinciding with the period of most intense water depletion (see Fig. 3). The relative decrease in the concentration of available IFN between 800 and 1000 m after 2100 UTC is associated with large ice nucleation rates and the presence of the maximum of the TCP curves

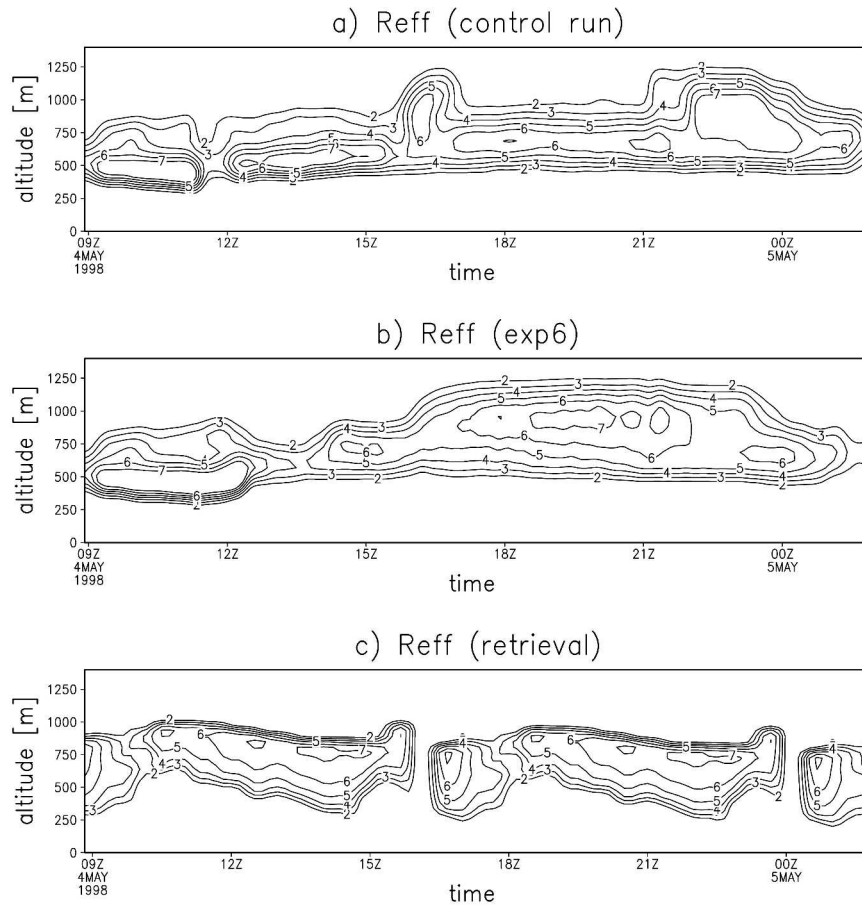


FIG. 4. Comparison of simulated and retrieved droplet effective radius (μm). (a) The control run and (b) the experiment that uses observed IFN/CCN profiles for initialization. (c) Plots of retrieved droplet effective radii. (Courtesy of P. Zuidema.)

(Fig. 6a). Figure 6c shows the differences in the long-wave downwelling radiation at the surface (LWDN) simulated in runs exp2, exp3, exp4, and exp5 with respect to the control run. The differences in the horizontally averaged LWDN are positive for all runs, indicating values larger than those of the control run. Note that LWDN differences are correlated with the total condensate paths (see Fig. 6a). However, the lowest values correspond to the period in which the simulated clouds glaciate. Figure 6d is a similar plot to Fig. 6c except for shortwave downwelling radiation at the surface (SWDN). It can be seen that SWDN differences are negative and clearly correlated with the depletion of the liquid water content.

Additional numerical experiments have been performed by varying initial IFN concentrations but assuming polluted CCN profiles above the inversion. The main results of Fig. 6 remain unaltered for different initial CCN concentrations (not shown). To isolate the effects of CCN entrainment, the simulated values of

LWC, IWC, and downwelling radiative fluxes have been compared for runs that differ in the initial CCN concentration above the inversion but assume the observed IFN profile for initialization. Figure 7 compares three runs for which the upper layer CCN concentration was initialized with 100, 250, and 500 cm^{-3} (exp4, exp6, and exp7, respectively) and the observed IFN profile. Differences of ice water path (IWP), liquid water path (LWP), LWDN, and SWDN for runs exp6 and exp7 with respect to exp4 are plotted in this figure. It can be seen that the time evolution of the horizontally averaged values of the above-mentioned quantities shows a much lower sensitivity to the initial CCN profile. Slightly higher LWP and SWDN values are associated with higher initial CCN concentrations. Conversely, IWP and LWDN differences are predominantly negative indicating lower values for runs that assume an upper layer more polluted on CCN. The sign and magnitude of these differences suggest that the CCN effect is opposite although less important than

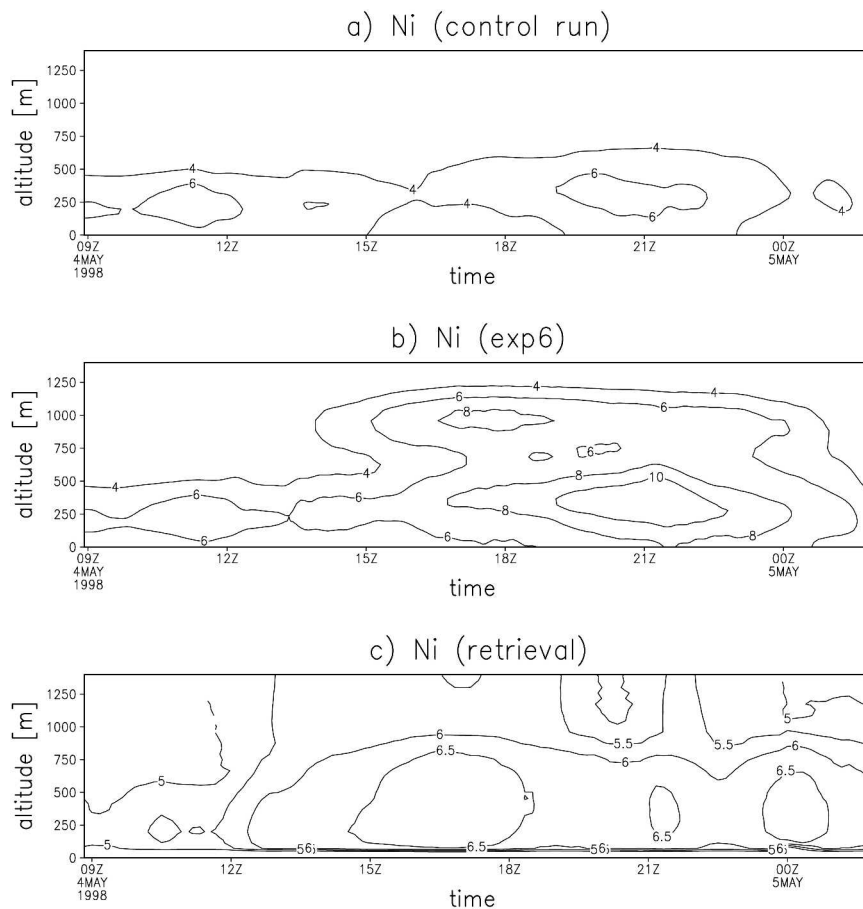


FIG. 5. Comparison of simulated and retrieved ice particle concentration (L^{-1}): (a) control run, (b) exp6, and (c) retrieved.

that associated with IFN entrainment. When comparing the runs that only differ in the initial CCN profile within the upper layer, the simulated droplet effective radius decreases with increasing CCN concentration (not shown).

The simulated precipitation rates also exhibit a monotonic increase when the initial IFN concentration above the inversion increases, as shown in Fig. 8a for the control run, exp2, exp3, exp4, and exp5. These curves present a pattern very similar to that of TCP (Fig. 6a), and exhibit maxima at the same time. However, while precipitation rates increase only 30%, TCP increases more than 60% when comparing the control run and exp4. The ratio between IWP and the precipitation rate can be considered an estimate of the residence time of the ice particles. This ratio is compared for the same set of experiments used in Figs. 8a and 8c. These curves suggest that residence times monotonically increase when upper layers are more polluted on IFN. The temporal evolution of the mean mass diameters corresponding to snow and aggregates is com-

pared in Figs. 8b and 8d, respectively. At the time at which the maximum precipitation rate is attained, both plots indicate smaller precipitating particles for the observed initial IFN profile compared to the control run. For the category associated with ice particles that only grow by vapor deposition and riming (snow), smaller particles prevailed during the period of significant precipitation rates.

5. Summary

In this paper we examine how the entrainment of aerosol from a polluted air layer overriding an inversion may affect the surface energy budget and the cloud microphysical structure of Arctic boundary layer clouds. For this study we used the cloud-resolving version of RAMS@CSU coupled with CICE along with a sophisticated bulk microphysical package. This new treatment of the microphysics includes the prognostic number concentration of cloud droplets via nucleation of CCN, which provides a more precise

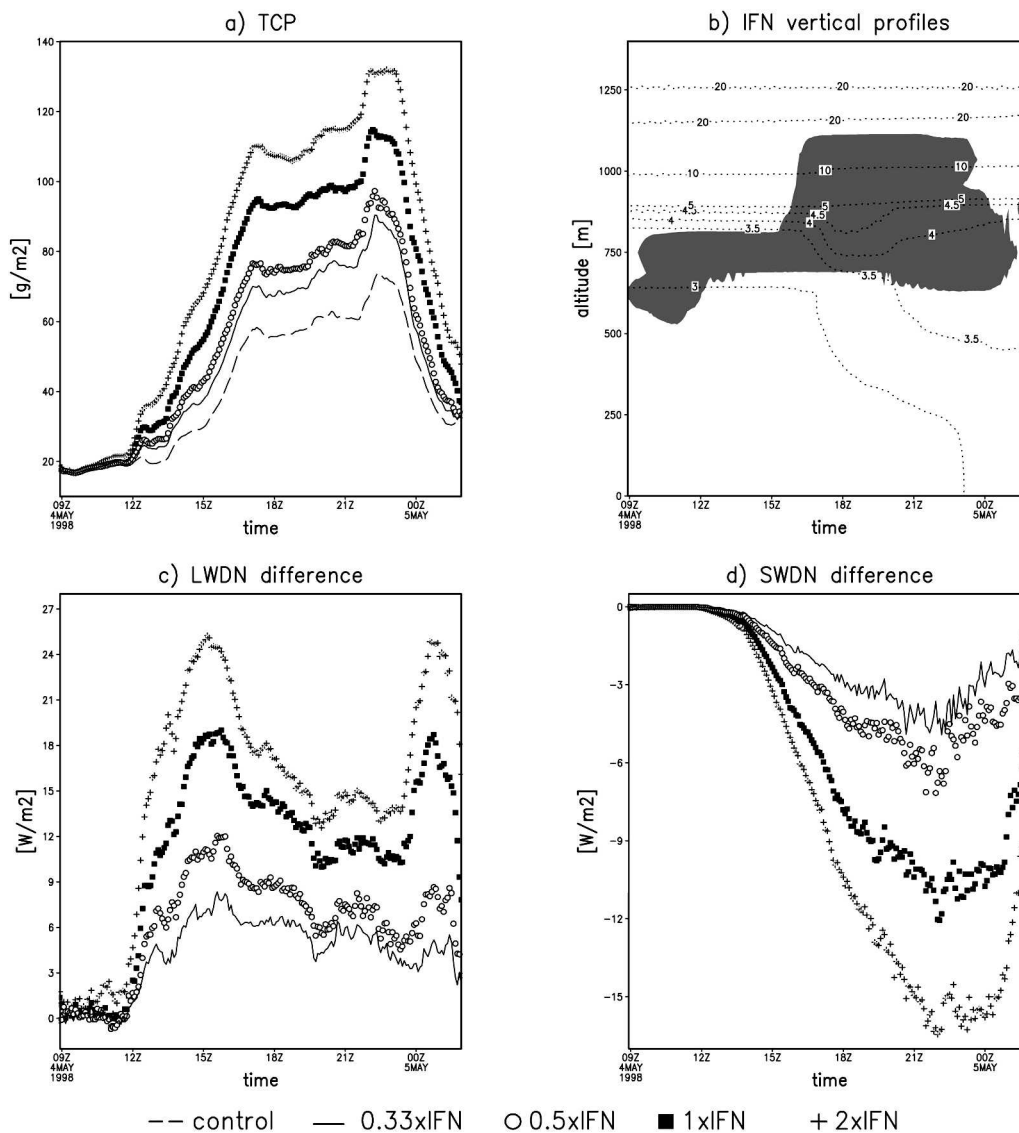


FIG. 6. Comparison of (a) TCP, (c) LWDN, and (d) SWDN for runs initialized with a clean CCN concentration and different IFN profiles. (b) Dotted lines represent the horizontally averaged concentration of available IFN (L^{-1}). The 0.001 g m^{-3} LWC contour has also been superimposed in (b) to indicate liquid cloud boundaries.

calculation of the amount of the droplet mass and number and also limiting cloud droplet nucleation depending upon available CCN. Additionally, the new microphysical module considers a new cloud mode that provides a more accurate representation of the bimodal distribution of cloud droplets that occurs in the atmosphere. Results from a series of CRM simulations of the 4 May 1998 mixed-phase cloud observed during the FIRE/SHEBA spring field campaign have been presented. To isolate the effects of IFN and CCN entrainment from a polluted upper layer, sensitivity experiments were initialized using different initial IFN

and CCN vertical profiles based on airborne aerosol data.

The main results of the present study can be summarized as follows: The entrainment of IFN at cloud top tends to increase the longwave downwelling radiation at the surface and the total condensate paths while decreasing liquid water paths. The increase of LWDN and TCP are clearly correlated and both quantities exhibit a monotonic behavior when more polluted upper layers were assumed for initialization. When we looked at the contribution of CCN entrainment, the current study is in agreement with Jiang et al. (2001), suggesting that its

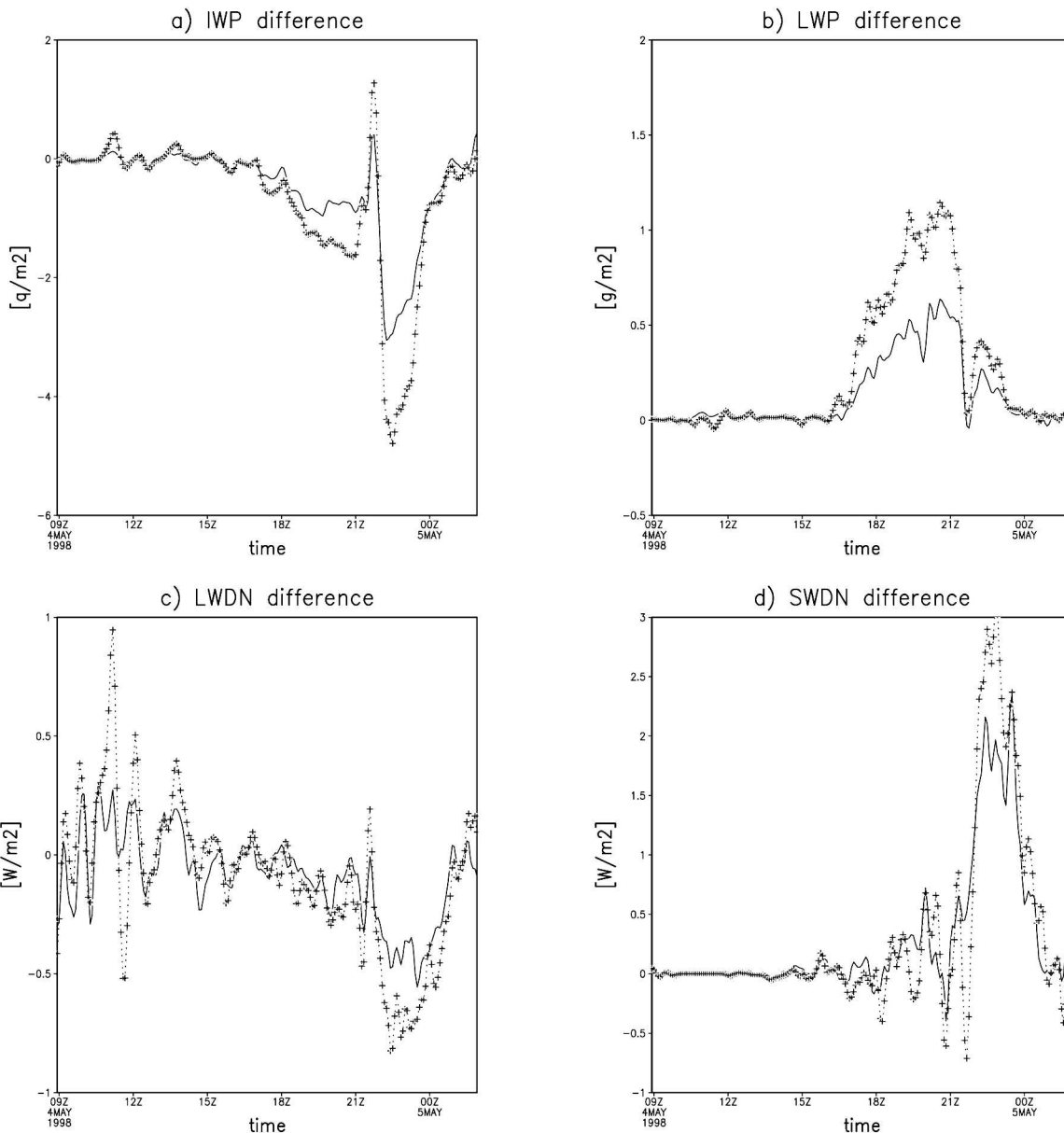


FIG. 7. Comparison of (a) IWP, (b) LWP, (c) LWDN, and (d) SWDN for runs initialized with the observed IFN profiles and different initial CCN concentrations. Solid lines indicate differences between the experiments that use observed and clean CCN concentrations for initialization (exp7 - exp4). Crosses denote differences between the runs initialized with twice the observed and clean CCN concentrations (exp8 - exp4).

effect is opposite although less important than that associated with IFN entrainment for this case.

For warmer cases, previous studies (see section 1) indicated that an increase in the IFN concentration can result in an optically thin layer and a reduction in LWDN mainly linked to liquid water depletion. The results of the sensitivity study presented in this paper indicate a different effect of IFN entrainment for colder cases. Precipitation of ice is not significant in this study largely because of the large number concentration of

ice particles in the polluted cases. More particles compete for the available vapor and therefore they are less likely to reach sizes to sediment as pristine crystals. On the other hand, even when an increased ice number concentration would increase the probability of binary interactions, smaller crystals will also be less efficient in colliding/aggregating. Therefore the significant increase in TCP (and in LWDN) is associated with an increase in the residence time of the ice particles.

In summary, the results presented here indicate that

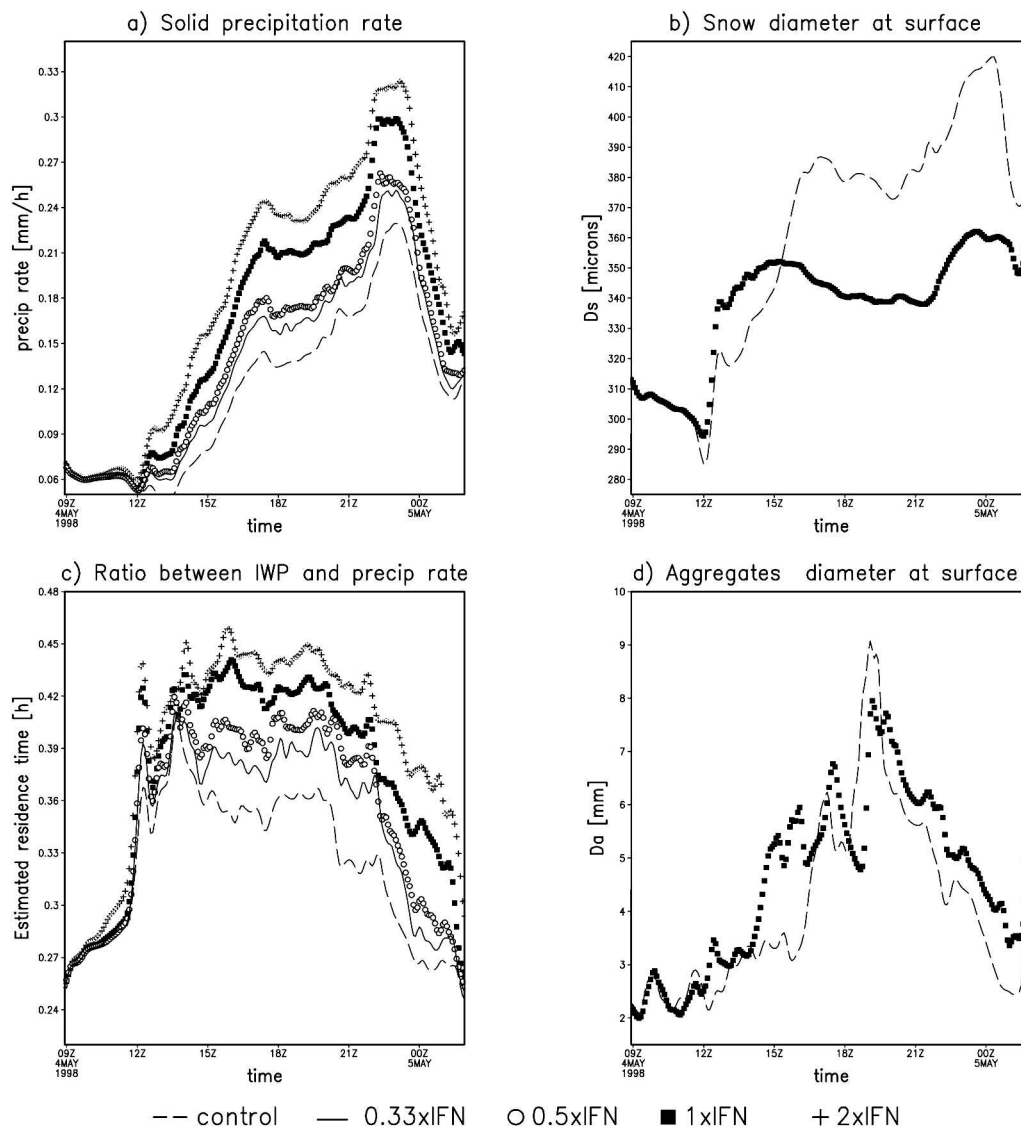


FIG. 8. (a) Comparison of solid precipitation rate, (c) the ratio between IWP and the precipitation rate, and (b), (d) the mean mass diameters of snow and aggregates for runs initialized with a clean CCN concentration and different IFN profiles.

entrainment of aerosol from above the inversion has an important impact on the microphysical structure of the simulated mixed-phase Arctic boundary layer cloud. Larger downwelling radiative fluxes at the surface suggest a potential enhancement of the sea ice melting rates. Further experiments were conducted to investigate the effect of aerosol intrusions on sea ice melting rates. Similar sensitivity studies have been performed for the spring–summer period of 1998 using 2 to 3 daily SHEBA soundings to provide time-evolving boundary conditions for the cloud-resolving model. Results of these multimonth CRM simulations are presented in Part II.

Future work will focus on considering intrusions that differentially enhance CCN concentrations with respect to those of IFN and vice versa. Along that line, we plan to study the impact of these intrusions from a larger-scale perspective using observational data to nudge aerosol concentrations.

Acknowledgments. This research was supported by a University of Alaska Fairbanks Research Contract UAF-00-0086/FP100092 and by NSF Grant ATM 0215367. The authors wish to thank Paquita Zuidema for providing cloud droplet size retrievals, Bill Lipscomb for providing the CICE code and consulting sup-

port on its use, Steve Saleeby for useful discussions, and Brenda Thompson for technical support.

REFERENCES

- Borys, J. R., and K. A. Rahn, 1981: Long-range transport of cloud-active aerosol to Iceland. *Atmos. Environ.*, **15**, 1491–1501.
- Carrió, G. G., H. Jiang, and W. R. Cotton, 2005: Impact of aerosol intrusions on Arctic boundary layer clouds. Part II: Sea ice melting rates. *J. Atmos. Sci.*, **62**, 3094–3105.
- Cotton, W. R., and Coauthors, 2003: RAMS 2001: Current status and future directions. *Meteor. Atmos. Phys.*, **82**, 5–29.
- Curry, J. A., and Coauthors, 2000: FIRE Arctic clouds experiment. *Bull. Amer. Meteor. Soc.*, **81**, 5–29.
- Feingold, G., and A. J. Heymsfield, 1992: Parameterizations of condensational growth of droplets for use in general circulation models. *J. Atmos. Sci.*, **49**, 2325–2342.
- Harrington, Y. Y., T. Reisin, W. R. Cotton, and S. M. Kreidenweis, 1999: Cloud resolving simulations of Arctic stratus. Part II: Transition-season clouds. *Atmos. Res.*, **51**, 45–75.
- Hunke, E. C., and W. M. Lipscomb, 1999: CICE: The Los Alamos Sea-Ice Model. Documentation and Software, Version 2.0.
- Jiang, H., W. R. Cotton, J. O. Pinto, J. A. Curry, and M. J. Weisbluth, 2000: Cloud resolving simulations of mixed-phase Arctic stratus observed during BASE: Sensitivity to concentration of ice crystals and large-scale heat and moisture advection. *J. Atmos. Sci.*, **57**, 2105–2117.
- , G. Feingold, W. R. Cotton, and P. G. Duynkerke, 2001: Large-eddy simulations of entrainment of cloud condensation nuclei into the Arctic boundary layer: May 18, 1998, FIRE/SHEBA case study. *J. Geophys. Res.*, **106D**, 15 113–15 122.
- Lipscomb, W. H., 2001: Remapping the thickness distribution of sea-ice. *J. Geophys. Res.*, **106**, 13 989–14 000.
- Meyers, M. P., R. L. Walko, J. Y. Harrington, and W. R. Cotton, 1997: New rams cloud microphysics parameterization: Part II. The two-moment scheme. *Atmos. Res.*, **45**, 3–39.
- Mitchell, D. L., A. Macke, and Y. Liu, 1996: Modeling cirrus clouds. Part II: Treatment of radiative properties. *J. Atmos. Sci.*, **53**, 2967–2988.
- Olsson, P. Q., and J. Y. Harrington, 2000: Dynamics and energetics of the cloudy boundary layer in simulations of off-ice flow in the marginal ice zone. *J. Geophys. Res.*, **105**, 11 889–11 899.
- , —, G. Feingold, W. R. Cotton, and S. M. Kreidenweis, 1998: Exploratory cloud-resolving simulations of boundary-layer Arctic stratus clouds. Part I: Warm-season clouds. *Atmos. Res.*, **47–48**, 573–597.
- Patterson, J. R., B. T. Marshall, and K. A. Rahn, 1982: Radiative properties of Arctic aerosol. *Atmos. Environ.*, **16**, 2967–2977.
- Perovich, D. K., and Coauthors, 1999: SHEBA: Snow and Ice Studies. CD-ROM. [Available from D. Perovich, CRREL, 72 Lyme Rd., Hanover, NH 03755.]
- Pielke, R. A., and Coauthors, 1992: A comprehensive meteorological modeling system—RAMS. *Meteor. Atmos. Phys.*, **49**, 69–91.
- Ritter, B., and J. F. Geleyn, 1992: A comprehensive radiation scheme for numerical weather prediction models with potential applications in climate simulations. *Mon. Wea. Rev.*, **120**, 303–325.
- Rogers, D. C., P. J. DeMott, and S. M. Kreidenweis, 2001: Airborne measurements of tropospheric ice-nucleating aerosol particles in the Arctic spring. *J. Geophys. Res.*, **106**, 15 053–15 063.
- Saleeby, S. M., and W. R. Cotton, 2004: A large-droplet model and prognostic number concentration of cloud droplets in the RAMS@CSU model. Part I: Module descriptions and supercell test simulations. *J. Appl. Meteor.*, **43**, 182–195.
- Slingo, A., and M. Schreckner, 1982: On shortwave properties of stratiform water clouds. *Quart. J. Roy. Meteor. Soc.*, **108**, 407–426.
- Yum, S. S., and J. G. Hudson, 2001: Vertical distributions of cloud condensation nuclei spectra over the springtime Arctic Ocean. *J. Geophys. Res.*, **106**, 15 045–15 052.
- Zuidema, P., and Coauthors, 2005: An Arctic springtime mixed-phase cloudy boundary layer observed during SHEBA. *J. Atmos. Sci.*, **62**, 160–176.